Enhanced triboelectric nanogenerators based on 2D smectite clay nanosheets with a strong intrinsic negative surface charge

Li, Wenjian; Yan, Feng; Xiang, Yinyu; Zhang, Wei; Loos, Katja; Pei, Yutao

Published in:
Nano energy

DOI:
10.1016/j.nanoen.2023.108487

Publication date:
2023

Nano Energy 112 (2023) 108487

Contents lists available at ScienceDirect

Nano Energy

journal homepage: www.elsevier.com/locate/nanoen

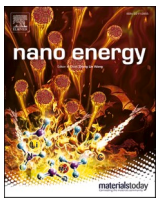

Enhanced triboelectric nanogenerators based on 2D smectite clay nanosheets with a strong intrinsic negative surface charge

Wenjian Li [a], Feng Yan [b], Yinyu Xiang [a], Wei Zhang [a], Katja Loos [c], Yutao Pei [a,*]

[a] Department of Advanced Production Engineering, Engineering and Technology Institute Groningen, Faculty of Science and Engineering, University of Groningen, Nijenborgh 4, 9747 AG Groningen, the Netherlands
[b] National Graphene Institute, University of Manchester, Manchester M13 9PL, UK
[c] Macromolecular Chemistry & New Polymeric Materials, Zernike Institute for Advanced Materials, Faculty of Science and Engineering, University of Groningen, Nijenbogh 4, 9747AG, Groningen, the Netherlands

ARTICLE INFO

Keywords:
Triboelectric nanogenerator
TENG
2D materials
Smectite clay

ABSTRACT

Triboelectric nanogenerators (TENGs) have demonstrated their huge potential in micro/nano energy harvesting for self-powered systems. The output performance of TENGs is largely dependent on the surface charge density of the triboelectric materials. Here, for the first time, we propose 2D smectite clay (SC) nanosheets with a strong intrinsic negative surface charge for improving the charge density of traditional triboelectric-negative materials. A single-layer 2D SC nanosheet (~1.1 nm thick) showed a strong negative surface potential (−14.3 mV), and the SC was confirmed to have a strong triboelectric negativity close to that of polytetrafluoroethylene (PTFE). 2D SC nanosheets were blended into polyvinylidene fluoride (SC-PVDF), based on which the SC-TENG demonstrated a significantly enhanced output performance, with the transferred charge increasing from 14 nC to 35 nC at the optimal SC concentration of 5 wt%. At higher SC concentrations, the influence of decreased effective contact area because of severe aggregation of SC nanosheets began to outperform the effect of increased interior charge. The instantaneous output power density of the SC-TENG was enormously improved to 1450 mW/m^2 from that of the pristine TENG (15 mW/m^2). This work proposed a new 2D material, SC, with a strong intrinsic negative surface charge, which has huge prospects in enhancing the output performance of TENGs.

1. Introduction

Micro/nano energy harvesting from the ambient environment provides a prospective power solution to realize self-powered systems in numerous fields, including self-powered sensor nodes in the distributed internet of things (IoT) [1–3], self-powered active sensors [4–6], and wearables [7–9]. Various kinds of high-entropy ambient energy [10], such as wind, vibration, human motion, water waves and raindrops, are almost completely wasted due to the lack of efficient energy harvesting techniques. Even though the efficiency of solar cells has been largely improved, they can work solely during sunny days. Electromagnetic and piezoelectric generators possess high output currents but confront low efficiency under low-frequency and low-amplitude stimuli [11,12]. Triboelectric nanogenerators (TENGs) [13,14], based on the coupling effect of contact electrification and electrostatic induction, have gained substantial attention since their invention for their higher energy conversion efficiency in low-frequency and random energy harvesting. The advantages of TENGs, including diverse structural designs, universal material choices, easy fabrication, low cost, and high efficiency, have enabled TENGs to be one of the most popular choices for energy harvesting and active sensing in many scenarios. Such high-entropy ambient wasted energy can be easily and effectively converted into electricity by TENGs as energy sources or active sensing information for self-powered systems [15]. The output performance of TENGs is largely dependent on the surface charge density of the triboelectric materials. As a result, improving the surface charge density of traditional materials is highly desired for enhanced TENGs. To date, many approaches, such as surface micropatterning [16], chemical modification [17], corona charge injection [18], and embedding of electron trapping materials [19], have been investigated to improve the surface charge density of triboelectric materials. However, these methods are somehow cumbersome, noncost-effective and short-term effective.

Smectite clay (SC), a natural mineral mixture of various swelling sheet silicates that is abundant on Earth, possesses a layer lattice

* Corresponding author.
E-mail address: y.pei@rug.nl (Y. Pei).

https://doi.org/10.1016/j.nanoen.2023.108487
Received 28 February 2023; Received in revised form 21 April 2023; Accepted 28 April 2023
Available online 5 May 2023

structure with weakened bonds between layers. The SC has a 2:1 layer (TOT) unit structure that consists of two SiO_2 tetrahedral (T) layers and an Al_2O_3 or Fe_2O_3 octahedral (O) central layer [20]. The TOT elementary layers are separated by an interlayer of hosting hydrated cations and water molecules, making it easy for SC to be exfoliated into 2D single-layer nanosheets. A negative surface charge is a natural characteristic of all SC minerals, ranging from 0.2 e to 0.6 e per half unit cell (corresponding to surface charge densities from −0.07 to −0.21 C/m^2) due to isomorphic substitutions of lower-charge cations for higher-charge cations in the octahedral or tetrahedral layers [21,22]. Compared with the triboelectric surface charges generated after contact electrification in TENGs, such a strong negative surface charge in SCs is intrinsic and eternal and is not affected by environmental factors. Therefore, it is highly interesting to investigate the triboelectric polarity of SC and composite SC into traditional triboelectric-negative materials to improve their total surface charge density. In addition, similar to other 2D materials (e.g., graphene, MXene, WS_2 and MoS_2) that have been widely applied in TENGs [23–26], the 2D structure of SC nanosheets indicates a large surface-to-volume ratio due to the atomic thickness and large lateral size, which can further increase the surface roughness and effective contact area of the triboelectric materials.

Herein, we proposed for the first time 2D SC nanosheets with a strong intrinsic negative surface charge for improving the surface charge density of traditional triboelectric-negative materials and thus enhancing the output performance of TENGs. The intrinsic negative surface charge of SC was first verified under a Kelvin probe force microscope (KPFM), in which a single-layer 2D SC nanosheet demonstrated a strong negative surface potential (−14.3 mV). Then, the triboelectric polarity of SC was investigated by comparison with three well-known triboelectric-negative materials, polyvinylidene fluoride (PVDF), polydimethylsiloxane

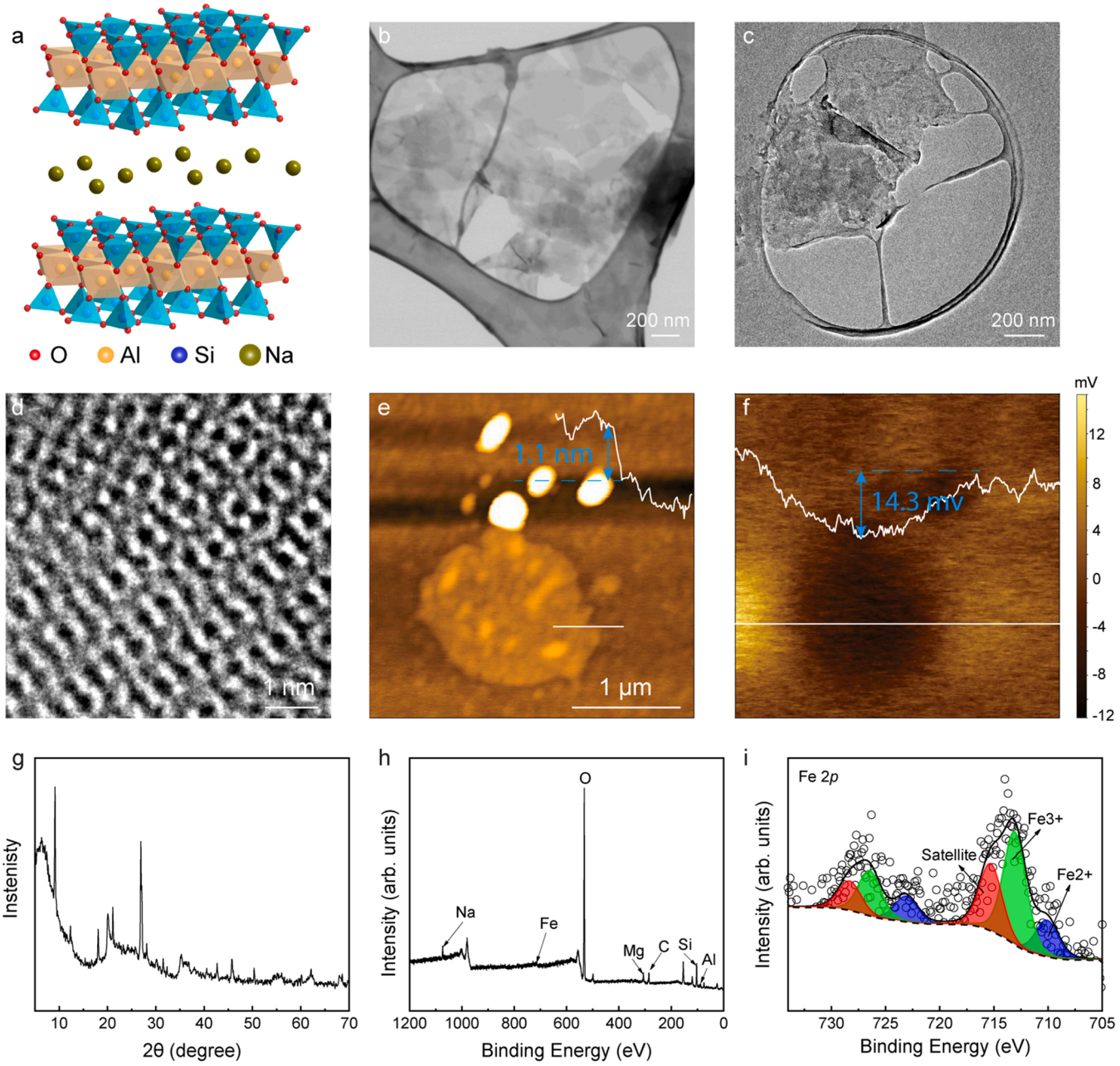

Fig. 1. Characterizations of the 2D SC nanosheets. (a) The 2:1 layer (TOT) unit structure of SC. (b) STEM image of SC nanosheets. (c) TEM image of a single-layer 2D SC nanosheet and (d) HRTEM image of its atomic structure. KPFM height (e) and surface potential distribution (f) of a single-layer SC nanosheet. (g) XRD pattern of the SC powders. (h) XPS survey spectra of SC nanosheets and (i) deconvoluted Fe 2p peak.

(PDMS) and polytetrafluoroethylene (PTFE). The results showed that SC was more tribelectrically negative than PVDF and PDMS but slightly more positive than PTFE. Therefore, 2D SC nanosheets were embedded into PVDF (SC-PVDF), which consequently demonstrated a higher TENG output (SC-TENG), with the transferred charge increasing from 14 nC to 35 nC with an optimal SC concentration of 5 wt%. The SC-TENG showed an increased output when the SC concentration increased to 5 wt%, after which the output gradually decreased due to the decreased effective contact area. The instantaneous output power density of the SC-TENG was enormously improved to 1450 mW/m^2 from that of the pristine TENG (15 mW/m^2), which means a 97-fold enhancement. LEDs and an electronic watch could be easily powered by the SC-TENG, demonstrating its huge potential in micro/nano energy harvesting for self-powered systems. This work proposed a new 2D material, SC, with strong triboelectric negativity, which has huge prospects in enhancing the surface charge density of traditional triboelectric negative materials.

2. Results and discussion

The schematic chemical structure and composition of the basic unit of SC is shown in Fig. 1a, which features a 2:1 layer (TOT) structure with two SiO_2 tetrahedral layers and an Al_2O_3 octahedral central layer. To ensure that SC sheets can be well dispersed into single- or few-layer nanosheets, sodium cations were chosen to intercalate into the smectite interlayers for their highest swelling ability of smectite. Fig. 1b shows the scanning transmission electron microscope (STEM) image of the SC after swelling, from which one can see that the SCs were well exfoliated into single- or few-layer nanosheets with ultrathin thickness. Fig. 1c is the transmission electron microscopy (TEM) image of a single-layer SC nanosheet, which shows that the SC nanosheet has a lateral size of approximately 1–2 μm. In addition, high-resolution TEM (HRTEM) (Fig. 1d) shows that SC nanosheets maintained a high crystalline and good structural order during swelling and exfoliation. Isomorphic substitutions of lower-charge cations for higher-charge cations in the octahedral or tetrahedral layers, for example, tetravalent silica, can be substituted by trivalent aluminum (Fig. S1), resulting in the net negative surface charge of SC. It has been reported that Na-intercalated SC solutions can have a negative zeta potential as high as − 45 mV [27]. KPFM measurements were conducted to prove the negative surface charge of the SC. As shown in Figs. 1e and 1f, even a single-layer SC nanosheet with a thickness of ~1.1 nm showed a strong negative surface potential of − 14 mV, proving the strong negative surface charge and potential of the SC. X-ray diffraction (XRD) spectra of the SC implied the purity of the SC used in this work (Fig. 1g). The chemical composition and isomorphic substitutions of the SC with interlayered sodium cations were characterized using X-ray photoelectron spectroscopy (XPS). The overview spectrum is shown in Fig. 1h, showing that all expected elements are present at the characteristic binding energy positions. Specifically, the presence of Mg and Fe indicates the isomorphic substitutions existing in the SC nanosheets. Fig. 1i shows the detailed spectrum of the Fe 2p peak, from which one can see that bivalent and trivalent iron substituted some higher-charge cations. In addition, the detailed spectra of other peaks, including Al, Si 2p, C 1 s, O 1 s and Na 1 s, are shown in Fig. S2.

The strong intrinsic negative surface charge of the SC suggests a potential strong triboelectric negativity during contact electrification, since the intrinsic negative charge can play a similar role as corona charge injection to improve the total charge density of polymers in TENGs. As a result, it is highly interesting to prove the strong triboelectric negativity of the SC by comparing its polarity with some well-known triboelectric-negative materials during contact electrification. Here, PVDF, PDMS, and PTFE were selected as counterpart materials for their strong triboelectric negativity. Typical contact-separation TENGs, which consist of the pure SC membrane and another counterpart material as the triboelectric pair, were fabricated, and their open-circuit voltage and short-circuit transferred charge were tested to determine the relative triboelectric polarity between the SC and counterparts according to a previously reported method [28]. As schematically depicted in Fig. S3, the SC membrane is assumed to be positively charged, and its backside copper electrode is connected to the positive probe of the electrometer (Fig. S3a) during measurement. In the open-circuit state (Fig. S3b), when the SC membrane separates from the counterpart material after contact electrification, a potential difference is then established between the two backside electrodes as the two triboelectric layers with opposite triboelectric charges are separated. Therefore, the open-circuit voltage will positively increase and reach its maximum when the separation distance reaches a certain value. In the short-circuit state (Fig. S3c), the potential difference can drive electrons flow from one electrode to the other. During separation, positive charges on the SC membrane can induce negative electrons on its backside electrode, so the electrons flow from the counterpart electrode to the SC electrode. Similarly, if the SC is negatively charged, a reverse change can be observed in the open-circuit voltage and short-circuit transferred charge.

The typical open-circuit voltage and short-circuit transferred charge of the contact-separation TENGs with the SC membrane and the other counterpart materials are shown in Fig. 2. In the case of SC and PVDF as triboelectric pairs, there was a negative peak in the open-circuit voltage (Fig. 2a) when the two materials separated from each other. The same phenomenon was observed in the short-circuit transferred charge (Fig. 2b). Therefore, it can be concluded that SC was negatively charged, while PVDF was positively charged. In other words, SC is relatively more tribelectrically negative than PVDF. Similarly, the SC is also relatively more triboelectric negative than the PDMS, as shown in Fig. 2c and d. In contrast, positive peaks were observed in the open-circuit voltage (Fig. 2e) and short-circuit transferred charge (Fig. 2f) during separation when PTFE served as the counterpart, which means that SC was positively charged and PTEF was negatively charged. However, the values of the maximum voltage and charge were just 3.8 V and 1.8 nC, respectively. In view of the common characteristic of the high output voltage of TENGs, such small values can indicate that the triboelectric negativity of the SC is very close to that of PTFE. To further verify the strong negativity of the SC nanosheets, surface potentials of the pure SC layer, PVDF, PDMS and PTFE were characterized under KPFM, and the results are shown in Fig. 2g. Compared with PVDF and PDMS, the pure SC showed a much higher negative potential of 0.91 V, which was close to that of PTFE (−1.13 V), revealing the strong triboelectric negativity of SC nanosheets. Therefore, the relative position of the SC in the triboelectric series can be approximately placed as illustrated in Fig. 2h, where SC is located at the strong negative side adjacent to PTFE. It is also worth noting that even though the output of PVDF (30 V) is smaller than that of PDMS (100 V), the relative position between PVDF and PDMS was determined based on previous results [28], as the output can be influenced by many factors, such as surface roughness, thickness and environmental humidity.

Although featured with strong triboelectric negativity, the pure SC membrane itself can hardly be used as an ideal triboelectric material because the SC membrane tends to easily crack and shatter due to its mineral properties. However, 2D SC nanosheets can work as modification materials to enhance the surface charge density of other triboelectric materials due to their large surface-to-volume ratio and intrinsic strong negative surface charge. Here, 2D SC nanosheets were blended into PVDF, and an SC-TENG with enhanced output performance using SC-PVDF as the triboelectric layer was fabricated. Certain contents of SC nanosheets were blended with PVDF solution and spin-coated on the Ti electrode that was deposited on an acrylic substrate. Another Ti layer was selected as both another triboelectric layer and electrode, as schematically illustrated in Fig. 3a. Blending of SC nanosheets led to a rough surface of the SC-PVDF, as seen from the SEM image of the surface morphology of the spin-coated SC-PVDF (Fig. 3b). Even some obvious surface uplift can be observed and probably caused by some SC nanosheets with large size, the SC nanosheets were still uniformly distributed

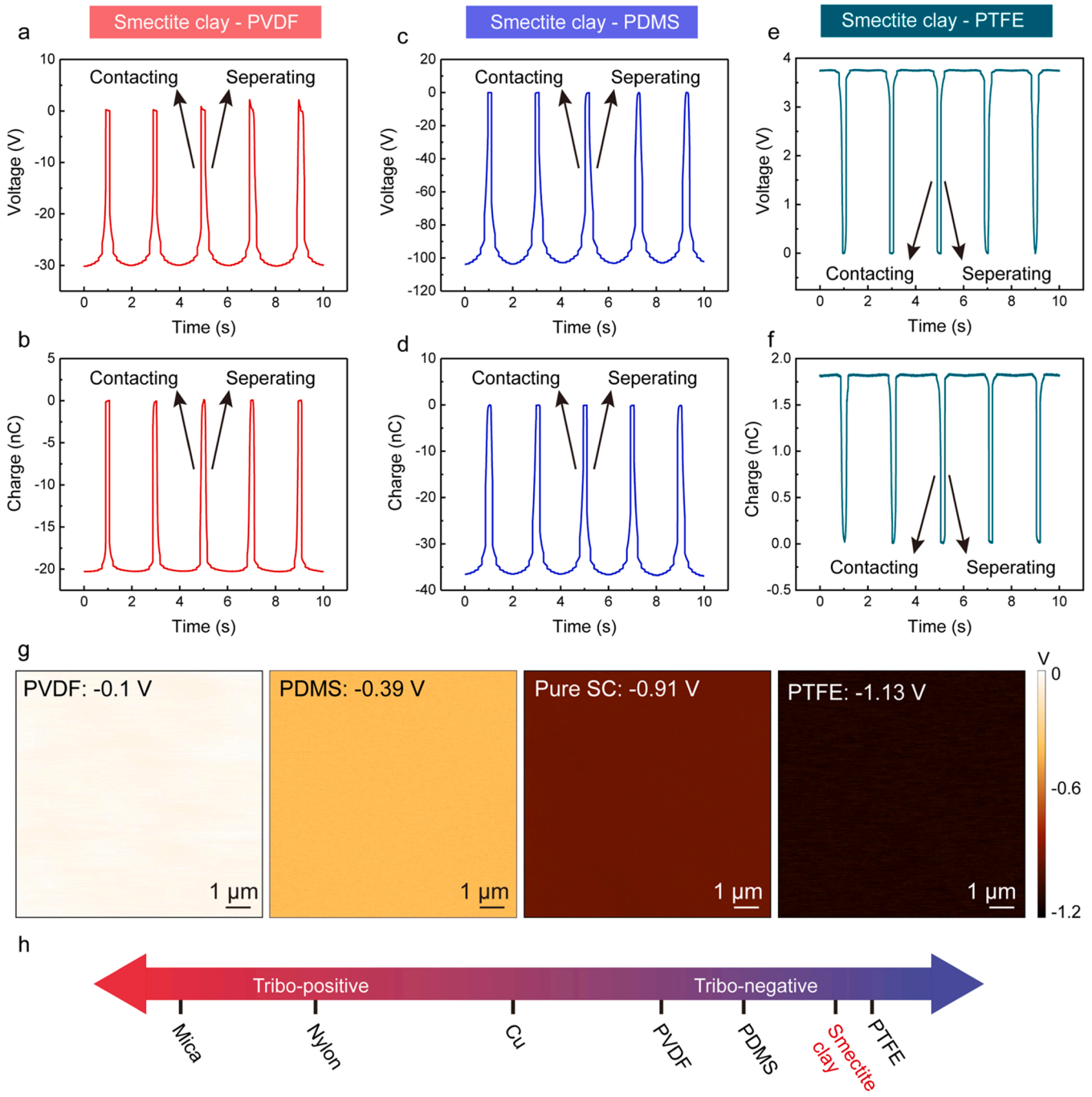

Fig. 2. Characterization of the triboelectric polarity of SC. Open-circuit voltage (a) and short-circuit transferred charge (b) with SC and PVDF as triboelectric pairs. Open-circuit voltage (c) and short-circuit transferred charge (d) with SC and PDMS as triboelectric pairs. short-circuit transferred charge (e) and short-circuit transferred charge (f) with SC and PTFE as triboelectric pairs. (g) Surface potential of PVDF, PDMS, SC and PTFE. (h) The position of the SC in the triboelectric series.

inside the SC-PVDF, as clearly proven by the energy dispersive spectrometry (EDS) elemental mapping (Fig. 3c). The surface potential of SC-PVDF showed a significant enhancement increased to − 0.56 V from − 0.1 V after adding 5 wt% of SC nanosheets (Fig. S4).

The working principle of the SC-TENG is illustrated in Fig. 3d. After several cycles of friction between the SC-PVDF and Ti, charges began to accumulate on the surfaces of the two triboelectric layers as a result of contact electrification. Due to their difference in the ability to attract and lose electrons, negative charges accumulated on the SC-PVDF surface, while equal amounts of positive charges accumulated on the top Ti electrode (state I). It is worth noting that the SC nanosheets in SC-PVDF were barely involved in contact electrification, which was almost dominated by PVDF. This is because the SC nanosheets were all wrapped by PVDF, since the XPS spectrum of SC-PVDF showed no elemental signal from the SC part (Fig. S5). As a result, the intrinsic negative charge in the SC nanosheets was permanently trapped as interior charges inside the SC-PVDF. Nevertheless, the intrinsic negative charges on SC nanosheets can increase the total charge density on the SC-PVDF, and thus enhance the electrostatic induction process. When the top Ti began to separate from the SC-PVDF, the strong negative charges on the SC-PVDF induced positive charges on its backside Ti electrode due to electrostatic induction, so electrons flowed from the bottom electrode to the top electrode (state II) until the negative charges on the SC-PVDF were fully balanced by the same amount of induced positive charges

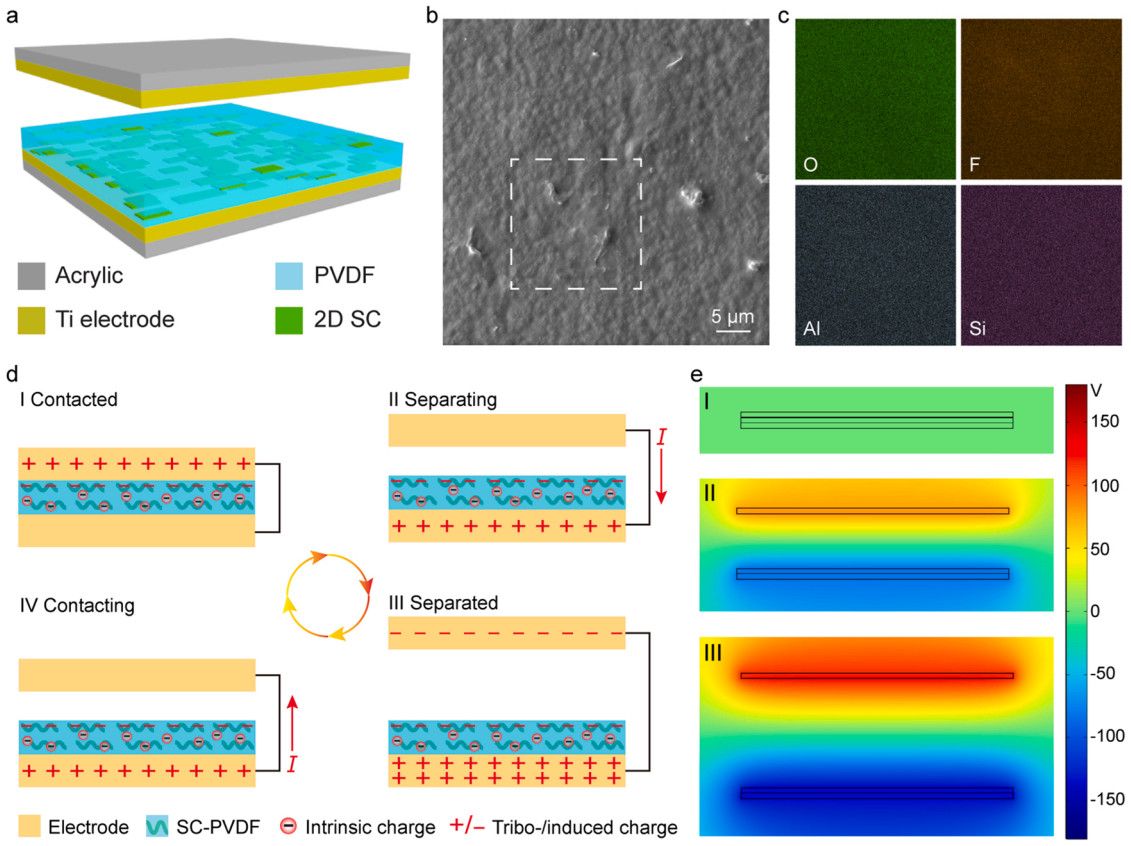

Fig. 3. Structure and working principle of the SC-TENG. a) Schematic structure of the SC-TENG. b) SEM image of the spin-coated SC-PVDF. c) EDS elemental mapping analysis of SC-PVDF. d) Schematic illustration of the working principle of the SC-TENG. e) Simulated electrical potential distribution of the SC-TENG during contact-separation.

(state III). Similarly, electrons flowed back from the top Ti electrode to the bottom electrode when the top Ti contacted the SC-PVDF again (state IV) until fully contacted (state I). Finite element analysis (FEA) was conducted using COMSOL Multiphysics software to simulate the electrical potential distribution of the SC-TENG during the three different states, as shown in Fig. 3e.

First, the influence of the concentration of the SC nanosheets in the SC-PVDF membrane on the output performance of the SC-TENG was investigated. Five different SC-PVDF samples with different SC concentrations, including 0, 2.5, 5, 7.5 and 10 wt%, were prepared. Fig. 4 a-c shows the output voltage, current, and transferred charge, respectively, of the SC-TENGs with the abovementioned varying SC concentrations. Unless otherwise indicated, the following working frequency and working load during the test were set as 0.5 Hz and 20 N, respectively. By introducing SC nanosheets into PVDF, the output of the SC-TENG showed a significant increase compared with that of the TENG with pristine PVDF (0 wt%). With the increased concentration of the SC nanosheets, the output of the SC-TENG first increased and reached a maximum at a concentration of 5 wt% and then showed a decreasing trend. At an SC concentration of 5 wt%, the output voltage, current and charge of the SC-TENG reached 104 V, 8.5 μA and 35 nC, respectively, while those of the pristine TENG were only 41.5 V, 1 μA, and 14 nC, respectively. Even when the concentration of the SC nanosheets further increased to 10 wt%, the output of the SC-TENG decreased, which was still almost 2 times that of the pristine TENG. The increase in the output of the SC-TENG after introducing the SC nanosheets was attributed to the additional negative surface charge in the SC, which can directly increase the total charge density of the SC-PVDF. To find out the cause behind the decrease in the output when the SC concentration exceeded 5 wt%, surface morphology and dielectric constant of SC-PVDF membranes were measured. As seen from Fig. 4 d, a uniform dispersion of SC nanosheets could be observed from the surface of PVDF at the SC concentration of 5 wt%, beyond which the SC nanosheets aggregated seriously and many SC bulks could be found. Fig. 4e and f demonstrate the measured dielectric constant and dielectric loss of SC-PVDF membranes. The dielectric constant of SC-PVDF slightly decreased from 8 to 5 when the SC content increased to 10 wt%. According to the equivalent capacitance model of TENG, such a slight change in the dielectric constant would have a negligible influence on the output performance of TENG. The dielectric loss of the SC-PVDF showed no significant increase after adding SC nanosheets despite of the high dielectric loss of pure SC. Therefore, the cause behind the decrease of output when the SC concentration exceeded 7.5 wt% was the severe aggregation of SC nanosheets. The aggregated SC bulks on the PVDF surface could cause regional high protrusions, which decreased the effective contact area of the PVDF. In addition to electrical properties, the influence of SC nanosheets on mechanical properties of SC-PVDF was also investigated. Fig. S6 shows the tensile test result of SC-PVDF membranes with different SC concentrations. When the SC concentration increased to 5 wt%, the maximum tensile strength increased from 18 MPa (pure PVDF) to 24.2 MPa (5 wt% SC-PVDF), after which the maximum tensile strength showed a decrease trend. It is worthy note that even the total strain of SC-PVDF decreases compared with that of pure PVDF, the elastic strains of SV-PVDF with 2.5 wt% and 5 wt% SC were almost the same as that of pure PVDF. For the following characterizations, the concentration of the SC nanosheets was selected as 5 wt%.

Then, the output performance of the SC-TENG under different working loads and frequencies was characterized. Fig. 4g demonstrates the output voltage of the SC-TENG under increased working loads, including 5, 10, 20, 30, 40, and 50 N, and Fig. 4h shows a summary of the corresponding output currents and charges. It is clear that the outputs of the SC-TENG increased obviously with the working loads,

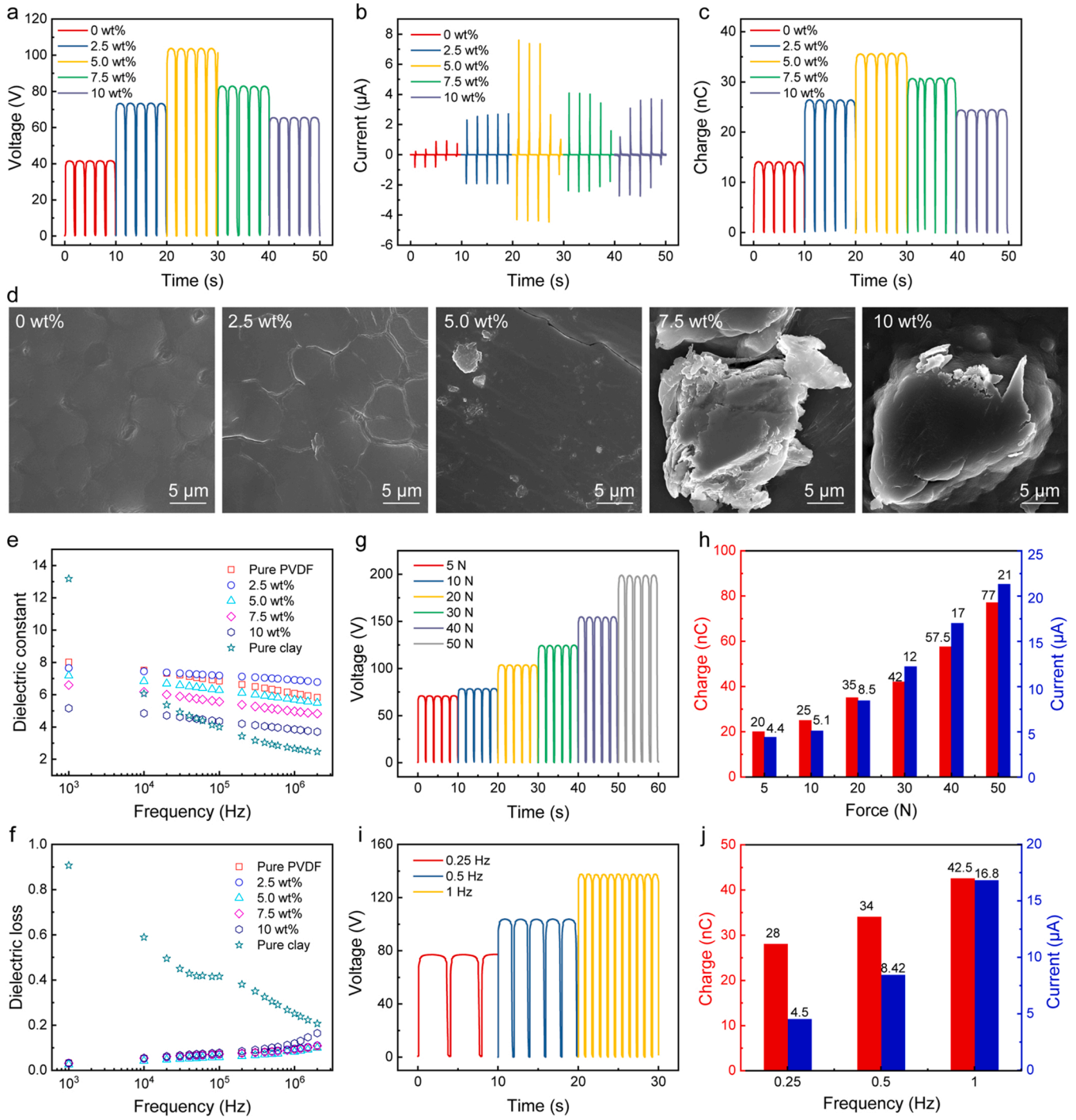

Fig. 4. Electrical characteristics of the SC-TENG. Open-circuit voltage (a), short-circuit current (b) and short-circuit transferred charge (c) of the SC-TENGs with different concentrations of SC nanosheets in the SC-PVDF. (d) SEM images of surface morphologies of SC-PVDF membranes with different SC concentrations. Measured dielectric constant (e) and dielectric loss (f) of SC-PVDF membranes with different concentrations of SC nanosheets. (g) Open-circuit voltage of the SC-TENG under different working loads. (h) Summary of the short-circuit current and transferred charge of the SC-TENG under different working loads. (i) Open-circuit voltage of the SC-TENG under different working frequencies. (j) Summary of the short-circuit current and transferred charge of the SC-TENG under different working frequencies.

increasing from 75 V at 5 N to 200 V at 50 N. As discussed above, the blending of 2D SC nanosheets into PVDF results in a rough surface morphology of SC-PVDF due to the large surface-to-volume ratio of its 2D structure. As the working load increased, the contact between the SC-PVDF and Ti electrode became more intimate, leading to an increased effective contact area and corresponding enhanced output. The output voltage of the SC-TENG under different working frequencies of 0.25, 0.5, and 1 Hz is shown in Fig. 4i. The changes in the output current and charge with working frequencies are also summarized in Fig. 4j. The current demonstrated a normal linear increase when the frequency increased from 0.25 to 1 Hz. Interestingly, the voltage and charge also slightly increased with increasing frequency. This was probably because of the more severe charge dissipation at lower frequencies due to the high dielectric loss of the SC, and surface charges can be quickly

replenished at higher frequencies.

The excellent output performance of the SC-TENG was expected to have a good resistance to environmental humidity since the enhancement was originated from the intrinsic strong negative surface charge in the SC nanosheets. As demonstrated in Fig. S7a and S7b, when the relative humidity (RH) increased from 30% to 90%, the output voltage of the pristine TENG with pure PVDF decreased from 50 V to 14 V, while that of the SC-TENG decreased from 108 V to 79 V. Setting the output voltage under the RH of 30% as 100%, the normalized voltages of the two TENGs under different RH are summarized in Fig. S7c, which clearly shows that the SC-TENG has a significantly improved humidity resistance compared with the pristine TENG.

Impedance matching measurements were conducted to determine the internal resistance and instantaneous output power density of the SC-TENG. In addition, the impedance matching of the pristine TENG was also measured for comparison. The output voltage and current of the SC-TENG and pristine TENG with different connected external resistors are demonstrated in Fig. 5a and b, respectively. The output voltage first gradually increased and then saturated when the external resistance increased, while the current first remained stable and then gradually decreased. The instantaneous output power densities of the SC-TENG and pristine TENG were correspondingly calculated and are shown in Fig. 5c. The SC-TENG possessed a maximum instantaneous output power density of 1452 mW/m^2 under an external resistance of 30 M, while the pristine TENG demonstrated a maximum instantaneous output power density of 15 mW/m^2 under an external resistance of 50 MΩ. This means that with the assistance of the 2D SC nanosheets, the instantaneous output power density of the SC-TENG was greatly enhanced by 97 times. It is then conceivable that the SC-TENG had a much faster charging speed when charging capacitors compared with the pristine TENG. As shown in Fig. 5d and e, capacitors of 1 μF and 4.7 μF were charged to 3 V by the SC-TENG in 52 and 124 s, respectively, while for the pristine TENG, it took 194 s and 488 s, respectively (working frequency 1 Hz). The SC-TENG also demonstrated excellent long-term stability, as shown in Fig. 5f, which shows the stable output charge of the SC-TENG over 10k cycles. The surface morphologies of pure PVDF and SC-PVDF were characterized before and after the test to compare their material durability. As shown in Fig. S8, the SC-PVDF showed an excellent material durability as there was no obvious change in the surface microstructure. On the contrary, some debris could be observed for the pure PVDF after

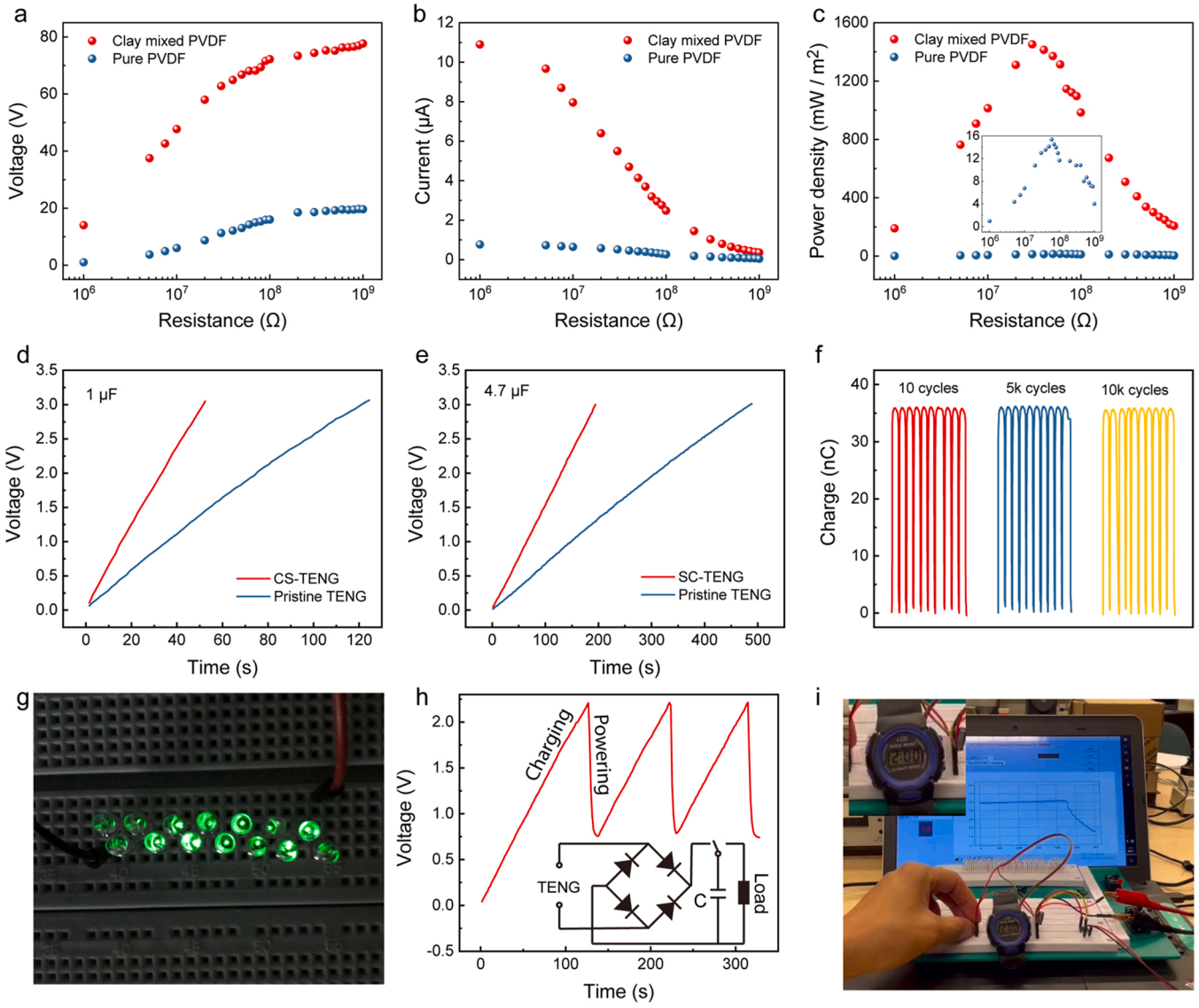

Fig. 5. Output power density and application of the SC-TENG. Output voltage (a) and current (b) of the SC-TENG with different external resistors. (c) Calculated instantaneous output power density of the SC-TENG. Charging 1 μF (d) and 4.7 μF (e) capacitors by the SC-TENG. (f) Long-term stability test of the SC-TENG. (g) Instantaneous lighting up 14 LEDs by the SC-TENG. (h) Powering an electronic watch by the SC-TENG. (i) Demonstration of powering the electronic watch.

test. With excellent output performance and stability, the SC-TENG is believed to have huge potential in micro/nano energy harvesting for self-powered systems. As demonstrated, 14 LEDs could be instantaneously lit up by the SC-TENG (working frequency: 1 Hz), as shown in Fig. 5g. In addition, the energy harvested by the SC-TENG can be effectively stored in a capacitor and then used to power some daily electronics. Fig. 5h demonstrates the voltage change of a 4.7 μF capacitor applied to store the harvested energy and then power an electronic watch by the SC-TENG (inset is the electrical connection diagram). The electronic watch could be easily powered by the SC-TENG every 100 s Fig. 5i and Video S1 show a photo of the powered watch and the detailed powering process.

Supplementary material related to this article can be found online at doi:10.1016/j.nanoen.2023.108487.

3. Conclusion

In conclusion, for the first time, we proposed 2D SC nanosheets with a strong intrinsic negative surface charge for enhanced TENGs. First, the strong intrinsic negative surface charge was verified by KPFM measurement, which showed that a single-layer 2D SC nanosheet had a strong negative surface potential. The SC was also confirmed to possess a strong triboelectric negativity, which is much more negative than PVDF and PDMS but slightly more positive than PTFE. At an SC concentration of 5 wt%, the SC-TENG showed the best output charge of 35 nC, while that of the pristine TENG was only 14 nC. The instantaneous output power density of the SC-TENG was greatly improved to 1452 mW/m^2, which is approximately 97 times that of the pristine TENG (15 mW/m^2). Daily electronics such as LEDs and electronic watches can be easily powered by the SC-TENG, demonstrating its huge potential in micro/nano energy harvesting for self-powered systems. This work proposed a new 2D material, smectite clay, with strong triboelectric negativity, which has huge prospects in enhancing the TECD of traditional triboelectric negative material.

4. Experiments

4.1. Preparation of 2D SC nanosheets

Smectite clay (montmonillonite, $(Na,Ca)_{0.3}(Al,Mg)_2Si_4O_{10}(OH)_2.nH_2O$) with a cation exchange capacity of 78 meq/100 g and flake size of 200 μm was obtained from the Source Clay Minerals Repository, Columbia. SC was purified with standard method used in clay science. Sodium exchanged SC was prepared by immersing the pristine clay in 1 N sodium chloride solution, washing it with distilled deionized water and transferring it to dialysis tubes in order to obtain chloride-free clay. Then, the obtained clay was dried for future usage.

4.2. Preparation of SC-PDVF solution

Certain weights of dried SC powders were first blended and swelled in Milli-Q water to obtain well-distributed single-layer and few-layer 2D SC nanosheets. Then, the solution was centrifuged at 10000 rpm for 10 min, and the supernatant was discarded. The remaining sediment was further ultrasonically dispersed in dimethylformamide (DMF, 99.9%, Sigma—Aldrich). Centrifugation, solvent replacement and ultrasonication were repeated 3 times to ensure that the water was fully replaced by DMF. The final obtained sediment was ultrasonically dispersed in 5 ml DMF. Hereafter, appropriate weights of PVDF powders were added into the above solution and magnetically stirred at 500 rpm at 60 °C overnight to obtain the SC-PVDF solution.

4.3. Fabrication of the SC-TENG

Ti electrodes were first deposited on acrylic substrates (25 ×25 ×2 mm) through magnetron sputtering deposition in a TEER UDP400/4 closed-field unbalanced magnetron sputtering system. The SC-PVDF solution was then spin-coated on the Ti electrode and dried at 60 ℃ for 1 h. Another acrylic substrate with a Ti electrode was assembled together with the abovementioned SC-PVDF with Ti facing the SC-PVDF. The pure SC triboelectric layer was prepared as follows. Purified and sodium exchanged SC nanosheets were first dispersed in Mili-Q water by continuously magnetic stirring for at least 48 h to ensure that SC bulks were well-exfoliated into single or few layer nanosheets, which was critical to the formation of SC triboelectric layer. Then, the solution was slowly dried in a glass petri dish at 60 ℃. Finally, the SC triboelectric layer was carefully removed from the glass petri.

4.4. Characterizations

X-ray diffraction (XRD) measurements were performed on a D8 Advance Bruker diffractometer with Cu K_α radiation ($\lambda = 1.5418$ Å), employing 1 0.25° divergent silt and a 0.125° anti-scattering slit. XRD spectra were recorded in the 2θ range from 5° to 80° with a step of 0.02° and a counting time of 2 s per step. X-ray photoelectron spectroscopy (XPS) was performed on a Surface Science Instruments SSX-100 spectrometer with a monochromatic Al K_α X-ray source (hv = 14.86.6 eV). Scanning electron microscopy (SEM) was performed on Lyra, Tescan. Transmission electron microscopy (TEM) was performed on JEOL JEM 2200FS operating at 200 keV. The dielectric constants of pure PVDF, SC-PVDF and pure clay membranes were calculated by measuring the capacitance of a parallel plate capacitor, in which a circular membrane (diameter: 12 mm) was sandwiched by two electrodes, using a Keysight LCR meter. The dielectric dissipation factor was directly read from the LCR meter. Kelvin probe force microscopy (KPFM) measurements were conducted on a Bruker Multimode 8 AFM system under ambient conditions. A Pt-coated silicon tip (cantilever resonance frequency: ~75 kHz; spring constant: 2.8 N/m) was applied in lift mode with a lift height of 40 nm to conduct the KPFM. The SC nanosheets were dropped on a silicon substrate that was grounded during measurement. The electrical output of the SC-TENG was measured using a Keithley electrometer (model 6514). The contact-separation process of the SC-TENG was controlled with a contact-separation distance of 5 mm by a universal testing machine (MTS 810 system) with adjustable applied force and frequency.

CRediT authorship contribution statement

Wenjian Li: Conceptualization, Methodology, Investigation, Data curation, Formal analysis, Validation, Visualization, Writing – original draft; **Feng Yan:** Methodology, Writing – review & editing; **Yinyu Xiang:** Methodology, Writing – review & editing. **Wei Zhang:** Methodology, Writing – review & editing. **Katja Loos:** Supervision, Writing – review & editing; **Yutao Pei:** Conceptualization, Funding acquisition, Supervision, Writing – review & editing.

Declaration of Competing Interest

The authors declare that they have no known competing financial interests or personal relationships that could have appeared to influence the work reported in this paper.

Data Availability

Data will be made available on request.

Acknowledgments

W. L. acknowledges the China Scholarship Council, P. R. China for his Ph.D. scholarship (CSC, No. 201904910781).

Appendix A. Supporting information

Supplementary data associated with this article can be found in the online version at doi:10.1016/j.nanoen.2023.108487.

References

[1] T. Sanislav, G.D. Mois, S. Zeadally, S.C. Folea, Energy harvesting techniques for internet of things (IoT), IEEE Access 9 (2021) 39530–39549.

[2] H. Jayakumar, K. Lee, W.S. Lee, A. Raha, Y. Kim, V. Raghunathan, in Proceedings of the 2014 international symposium on Low power electronics and design, 2014, 375–380.

[3] W. Li, Y. Liu, S. Wang, W. Li, G. Liu, J. Zhao, X. Zhang, C. Zhang, Vibrational triboelectric nanogenerator-based multinode self-powered sensor network for machine fault detection, IEEE/ASME Trans. Mechatron. 25 (2020) 2188–2196.

[4] G. Khandelwal, R. Dahiya, Self-powered active sensing based on triboelectric generators, Adv. Mater. 34 (2022), e2200724.

[5] S. Wang, L. Lin, Z.L. Wang, Triboelectric nanogenerators as self-powered active sensors, Nano Energy 11 (2015) 436–462.

[6] W. Li, G. Liu, D. Jiang, C. Wang, W. Li, T. Guo, J. Zhao, F. Xi, W. Liu, C. Zhang, Interdigitated electrode-based triboelectric sliding sensor for security monitoring, Adv. Mater. Technol. 3 (2018) 1800189.

[7] P. Tan, Y. Zou, Y. Fan, Z. Li, Self-powered wearable electronics, Wearable Technol. 1 (2020), e5.

[8] Y. Zhou, X. Xiao, G. Chen, X. Zhao, J. Chen, Self-powered sensing technologies for human Metaverse interfacing, Joule 6 (2022) 1381–1389.

[9] W. Li, L. Lu, A.G.P. Kottapalli, Y. Pei, Bioinspired sweat-resistant wearable triboelectric nanogenerator for movement monitoring during exercise, Nano Energy 95 (2022), 107901.

[10] Z.L. Wang, Entropy theory of distributed energy for internet of things, Nano Energy 58 (2019) 669–672.

[11] J. Zhao, G. Zhen, G. Liu, T. Bu, W. Liu, X. Fu, P. Zhang, C. Zhang, Z.L. Wang, Remarkable merits of triboelectric nanogenerator than electromagnetic generator for harvesting small-amplitude mechanical energy, Nano Energy 61 (2019) 111–118.

[12] Y. Zi, H. Guo, Z. Wen, M.H. Yeh, C. Hu, Z.L. Wang, Harvesting low-frequency (<5 Hz) irregular mechanical energy: a possible killer application of triboelectric nanogenerator, ACS Nano 10 (2016) 4797–4805.

[13] Z.L. Wang, Triboelectric nanogenerator (TENG)—sparking an energy and sensor revolution, Adv. Energy Mater. 10 (2020) 2000137.

[14] F.-R. Fan, Z.-Q. Tian, Z. Lin Wang, Flexible triboelectric generator, Nano Energy 1 (2012) 328–334.

[15] B. Chen, Z.L. Wang, Toward a new era of sustainable energy: advanced triboelectric nanogenerator for harvesting high entropy energy, Small 18 (2022), e2107034.

[16] J. Huang, X. Fu, G. Liu, S. Xu, X. Li, C. Zhang, L. Jiang, Micro/nano-structures-enhanced triboelectric nanogenerators by femtosecond laser direct writing, Nano Energy 62 (2019) 638–644.

[17] Y. Liu, J. Mo, Q. Fu, Y. Lu, N. Zhang, S. Wang, S. Nie, Enhancement of triboelectric charge density by chemical functionalization, Adv. Funct. Mater. 30 (2020) 2004714.

[18] T. Zhou, L. Zhang, F. Xue, W. Tang, C. Zhang, Z.L. Wang, Multilayered electret films based triboelectric nanogenerator, Nano Res 9 (2016) 1442–1451.

[19] H. Jiang, H. Lei, Z. Wen, J. Shi, D. Bao, C. Chen, J. Jiang, Q. Guan, X. Sun, S.-T. Lee, Charge-trapping-blocking layer for enhanced triboelectric nanogenerators, Nano Energy 75 (2020), 105011.

[20] I.E. Odom, Smectite clay minerals: properties and uses, Philos. Trans. R. Soc. Lond. Ser. A 311 (1984) 391–409.

[21] L. BAILEY, H.N.W. LEKKERKERKER, G.C. MAITLANDC, Smectite clay – inorganic nanoparticle mixed suspensions: phase behaviour and rheology, Soft Matter 00 (2014) 1–3.

[22] P. Leroy, A. Revil, A triple-layer model of the surface electrochemical properties of clay minerals, J. Colloid Interface Sci. 270 (2004) 371–380.

[23] X. Xia, J. Chen, G. Liu, M.S. Javed, X. Wang, C. Hu, Aligning graphene sheets in PDMS for improving output performance of triboelectric nanogenerator, Carbon 111 (2017) 569–576.

[24] Y. Dong, S.S.K. Mallineni, K. Maleski, H. Behlow, V.N. Mochalin, A.M. Rao, Y. Gogotsi, R. Podila, Metallic MXenes: a new family of materials for flexible triboelectric nanogenerators, Nano Energy 44 (2018) 103–110.

[25] C. Wu, T.W. Kim, J.H. Park, H. An, J. Shao, X. Chen, Z.L. Wang, Enhanced triboelectric nanogenerators based on MoS(2) monolayer nanocomposites acting as electron-acceptor layers, ACS Nano 11 (2017) 8356–8363.

[26] T.I. Kim, I.J. Park, S. Kang, T.S. Kim, S.Y. Choi, Enhanced triboelectric nanogenerator based on tungsten disulfide via thiolated ligand conjugation, ACS Appl. Mater. Interfaces 13 (2021) 21299–21309.

[27] M. Chorom, P. Rengasamy, Dispersion and zeta potential of pure clays as related to net particle charge under varying pH, electrolyte concentration and cation type, Eur. J. Soil Sci. 46 (1995) 657–665.

[28] H. Zou, Y. Zhang, L. Guo, P. Wang, X. He, G. Dai, H. Zheng, C. Chen, A.C. Wang, C. Xu, Z.L. Wang, Quantifying the triboelectric series, Nat. Commun. 10 (2019) 1427.